Durability of Pt-Co Alloy Polymer Electrolyte Fuel Cell Cathode Catalysts under Accelerated Stress Tests

D. D. Papadias,[1,z] R. K. Ahluwalia,[1] N. Kariuki,[1] D. Myers,[1,*] K. L. More,[2,*]
D. A. Cullen,[2,*] B. T. Sneed,[2] K. C. Neyerlin,[3] R. Mukundan,[4,**] and R. L. Borup[4,*]

[1]*Argonne National Laboratory, Argonne, Illinois, USA*
[2]*Oak Ridge National Laboratory, Oak Ridge, Tennessee, USA*
[3]*National Renewable Energy Laboratory, Golden, Colorado, USA*
[4]*Los Alamos National Laboratory, Los Alamos, New Mexico, USA*

The durability of Pt-Co alloy cathode catalysts supported on high surface area carbon is investigated by subjecting them to accelerated stress tests (ASTs). The catalysts had different initial Co contents and nanoparticle morphologies: a "spongy" porous morphology for the high-Co (H) content catalyst, and a fully alloyed crystalline morphology for the medium-Co (M) and low-Co (L) content catalysts. The specific activity of the catalysts depends on their initial Co content, morphology and nanoparticle size, and remained higher than 1000 $\mu A/cm^2$-Pt after 27–50% Co loss. The H-catalyst electrode showed the smallest kinetic overpotentials (η_s^c) due to higher initial Pt loading than the other two electrodes, but it had the fastest increase in η_s^c with AST cycling due to lower Co retention; the L-catalyst electrode showed higher η_s^c due to a lower initial Pt loading, but had a smaller increase in η_s^c with aging due to higher Co retention; the M-catalyst electrode showed a similar increase in η_s^c with aging, but this increase was due to the combined effects of Co dissolution and electrochemically active surface area (ECSA) loss. The modeled increase in mass transfer overpotentials with aging correlates with the initial Pt loading, ECSA loss and the initial catalyst morphology.
© The Author(s) 2018. Published by ECS. This is an open access article distributed under the terms of the Creative Commons Attribution Non-Commercial No Derivatives 4.0 License (CC BY-NC-ND, http://creativecommons.org/licenses/by-nc-nd/4.0/), which permits non-commercial reuse, distribution, and reproduction in any medium, provided the original work is not changed in any way and is properly cited. For permission for commercial reuse, please email: oa@electrochem.org. [DOI: 10.1149/2.0171806jes]

(cc) BY-NC-ND

Over the past decade, the intrinsic oxygen reduction reaction (ORR) activity of platinum-based nanoparticle catalysts for polymer electrolyte fuel cells (PEFCs) has been improved by over an order of magnitude, with numerous catalysts now exceeding the catalytic activity target (>440 mA/mg$_{Pt}$) established for the automotive propulsion power application.[1–3] These high activities are typically achieved by alloying Pt with a transition metal (TM), such as Co, Ni, or Fe.[3] Many Pt-TM alloy nanoparticle catalysts are commercially available today, with a commercial Pt-Co catalyst reported being used in the Toyota Mirai fuel cell vehicle.[4,5] However, many of the high activity Pt-TM alloy catalysts exhibit poor durability in the membrane electrode assembly (MEA) environment, which is characterized by extensive leaching of the TM from the alloy nanoparticles into the cathode catalyst layer ionomer and the adjoining membrane.[2,6–10]

The objectives of this work are to develop an understanding of the stability of TMs in Pt-alloy catalysts, particularly the relationship between stability and the initial TM content and catalyst nanoparticle structure, and to understand the effect of TM leaching on the catalyst ORR activity and transport of oxygen to catalyst nanoparticles in the cathode. Our approach is to obtain meaningful results by conducting the study using state-of-the-art (SOA) Pt-alloy cathode catalysts in optimized electrodes and MEAs.

Experimental

Materials.—SOA Pt-Co alloy catalyst nanoparticles supported on high surface area carbon (HSAC), and MEAs fabricated from Pt-Co/HSAC were supplied by three sources: IRD (now EWii) Fuel Cells (IRD CAT0023) – catalyst H, Umicore (Elyst Pt30 0670) – catalyst M, and General Motors (GM) – catalyst L. The characteristics of each of the catalyst powders and MEAs used in this study are listed in Table I. The Pt:Co molar ratios listed in Table I were

determined using energy dispersive X-ray spectroscopy (EDS) in a scanning transmission electron microscope (STEM).[11] As shown in Table I, each catalyst incorporated in the MEA had a different initial average Co content, e.g., 34, 20, and 15 mol%, as measured in the cathode catalyst layer (CCL), for catalysts H, M, and L, respectively. Catalysts H and M were supplied as powders. Catalyst H was incorporated into the cathode catalyst layer of an MEA fabricated by IRD Fuel Cells at a loading 0.2 mg-Pt/cm². Catalyst M was made into an ink and MEAs were fabricated in-house using an ultrasonic spray coating technique with a cathode catalyst loading of 0.1 mg-Pt/cm². Catalyst L was received only as an MEA fabricated by General Motors (GM) with a CCL loading of 0.1 mg-Pt/cm². The high-angle annular dark-field (HAADF)-STEM images in Fig. 1 clearly show that each of these catalysts had a different nanoparticle size and morphology. Catalyst H exhibited a "spongy" porous (hollow) crystalline morphology with ~7 nm mean Pt-Co particle size after MEA conditioning; Catalyst M exhibited a fully alloyed, dense crystalline morphology with ~4.4 nm mean Pt-Co particle size after MEA conditioning; and Catalyst L had a fully alloyed, dense crystalline morphology with a ~4.5 nm mean Pt-Co particle size. None of these catalysts exhibited any structural (lattice) ordering or elemental segregation (e.g., core-shell).

Testing and characterization.—The MEAs were assembled with SGL 25BC gas diffusion layers (GDLs). MEAs were tested using a 50 cm² test cell with single channel serpentine flow fields, which was controlled by a fuel cell test stand (Fuel Cell Technologies, Albuquerque, NM). An accelerated stress test (AST) recommended by the U.S. Department of Energy Fuel Cell Technologies Office[12] was used to evaluate the durability of the cathode electrocatalysts. The AST utilizes a nitrogen sweep gas on the cathode and a hydrogen sweep gas on the anode, and 30,000 square wave cycles with a 0.6 V cathode lower potential limit (LPL), 0.95 V cathode upper potential limit (UPL), and 3 s holds at both LPL and UPL. The cell conditions were 80°C, 1 atm, and 100% relative humidity (RH) for both hydrogen and nitrogen, with flow rates of 200 sccm and 75 sccm, respectively. Changes in cell performance were monitored by measuring polarization in H₂-air, high frequency resistance

Table I. MEA and catalyst powder characteristics.

| Catalyst Designation	Supplier	Powder Pt:Co molar ratio	CCL Pt:Co	Membrane	L_{Pt} (mg/cm^2)	ECSA (m^2/g)
Catalyst H	IRD	60:40	66:34	Reinforced	0.21	41
Catalyst M	Umicore	70:30	80:20	Nafion 211	0.10	37
Catalyst L	GM	N/A	85:15	DuPont XL-100	0.10	43

(HFR), electrochemically-active surface area (ECSA), impedance in air and helox (79% He, 21% O_2), and mass activity. These measurements were made at beginning of test (BOT) and after 1000 (1 k), 5,000 (5 k), 10,000 (10 k), 20,000 (20 k) and 30,000 (30 k) cycles, i.e., at end of test (EOT).

ECSA was determined from hydrogen under-potential deposition (H_{upd}) in cyclic voltammetry (CV) between 0.085 and 0.65 V (vs. reversible hydrogen electrode (RHE)) at 80°C, 2.7 atm, and 20 mV/s scan rate. The H_2 crossover rate was evaluated under the same test conditions as the ECSA measurements.

The cell polarization curves were measured with H_2/air at 80°C and 100% RH. The cell backpressure was 2.8 atm and the flow rates were adjusted for stoichiometric ratios of 1.2 at the anode and 2.0 at the cathode, for current densities exceeding 0.2 A/cm^2. At lower current densities, the anode and cathode flow rates (on a dry basis) were kept constant at 42 sccm and 166 sccm, respectively. All polarization tests were obtained by varying the cell potential with 30 s hold times, starting from open circuit voltage (OCV) to 0.8 V in increments of 20 mV and from 0.8 V to 0.3 V in increments of 50 mV, followed by an up-scan to OCV.

Mass activities were measured in H_2/O_2 at 80°C, 100% RH, and 150 kPa absolute back pressure. Measurements were made by first reducing the cathode at 0.1 V for 15 min. under a H_2/N_2 environment, switching the cathode flow to O_2, and holding the potential at 900 mV for an additional 15 min. Mass activities were evaluated based on the average iR and H_2 crossover-corrected current during the last minute of the potential hold.

X-ray scattering characterization.—The catalyst particle sizes and d-spacing of atomic planes within the catalysts particles were determined using X-ray scattering at beam line 9-ID at the Advanced Photon Source at Argonne National Laboratory. The cathode layers from the CCMs were transferred onto Scotch tape using a simple press-peel technique and characterized using monochromatic X-rays ranging in energies from 16.8 to 21 keV. The scattered X-ray intensity was obtained over a range of scattering angles/scatterer dimensions using the combined ultra small-angle X-ray scattering (USAXS), pinhole small-angle X-ray scattering (pinSAXS), and wide-angle X-ray scattering (WAXS) using the combination of a Bonse-Hart camera for USAXS and a Pilatus 100 K detector for pinhole SAXS and WAXS. The complete scattered intensity, I(q), was then obtained by combining the USAXS (10^{-4} to 6×10^{-2} Å^{-1}) and the pinhole SAXS (3×10^{-2} to 1 Å^{-1}). The WAXS data covered a d-spacing range from approximately 6 Å to 0.8 Å. The background scattering from Scotch tape was collected and subtracted from the scattering data for each CCL sample. The combined USAXS-SAXS data analysis utilized Irena, a suite of macros written for the Igor Pro software platform by Jan Ilavsky of Argonne National Laboratory. The SAXS scattering data were fit with a lognormal distribution in the Q range of 0.03 to 0.40 Å^{-1} to obtain catalyst particle size distributions. This Q range corresponds to a particle size range of ~1.5 to 18 nm. The fit assumed the catalyst particles to be poly-dispersed spheres, which is the morphology consistent with the STEM images shown in Fig. 1. The WAXS data analysis utilized powder diffraction multi peak fitting 2.0, an Irena macro.
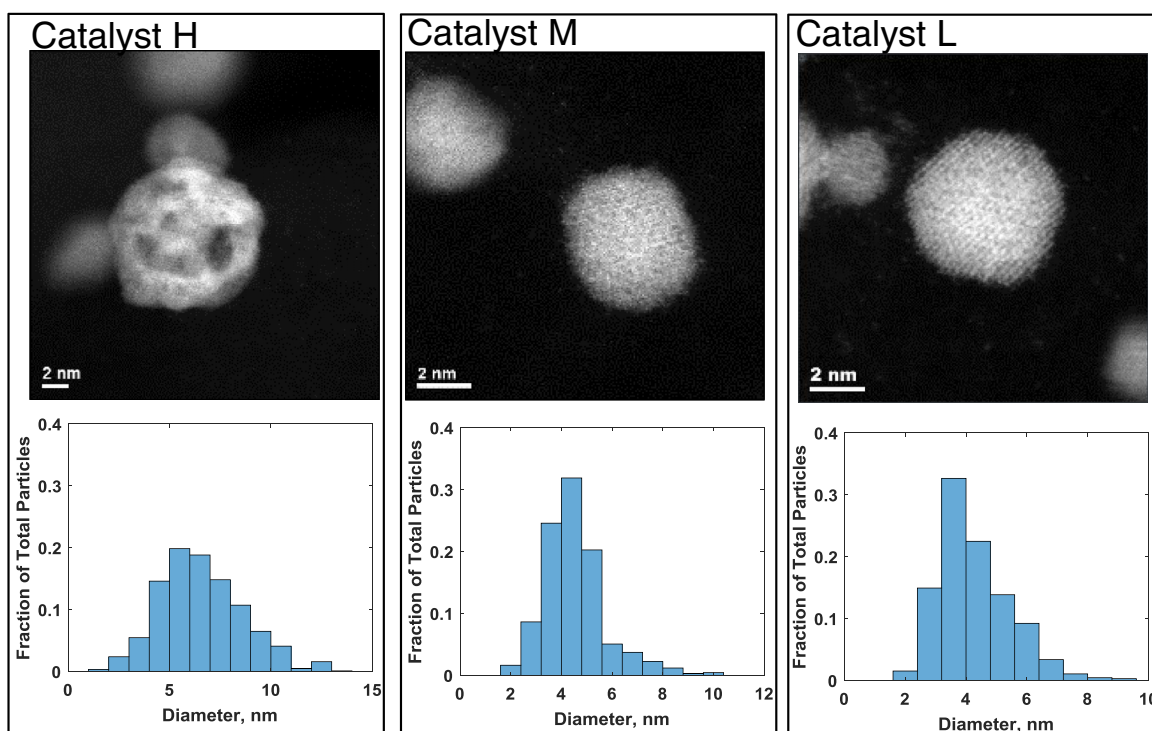
Figure 1. HAADF-STEM images of catalyst morphologies and particle size distributions for IRD catalyst H (left), Umicore catalyst M (center), and GM catalyst L (right).
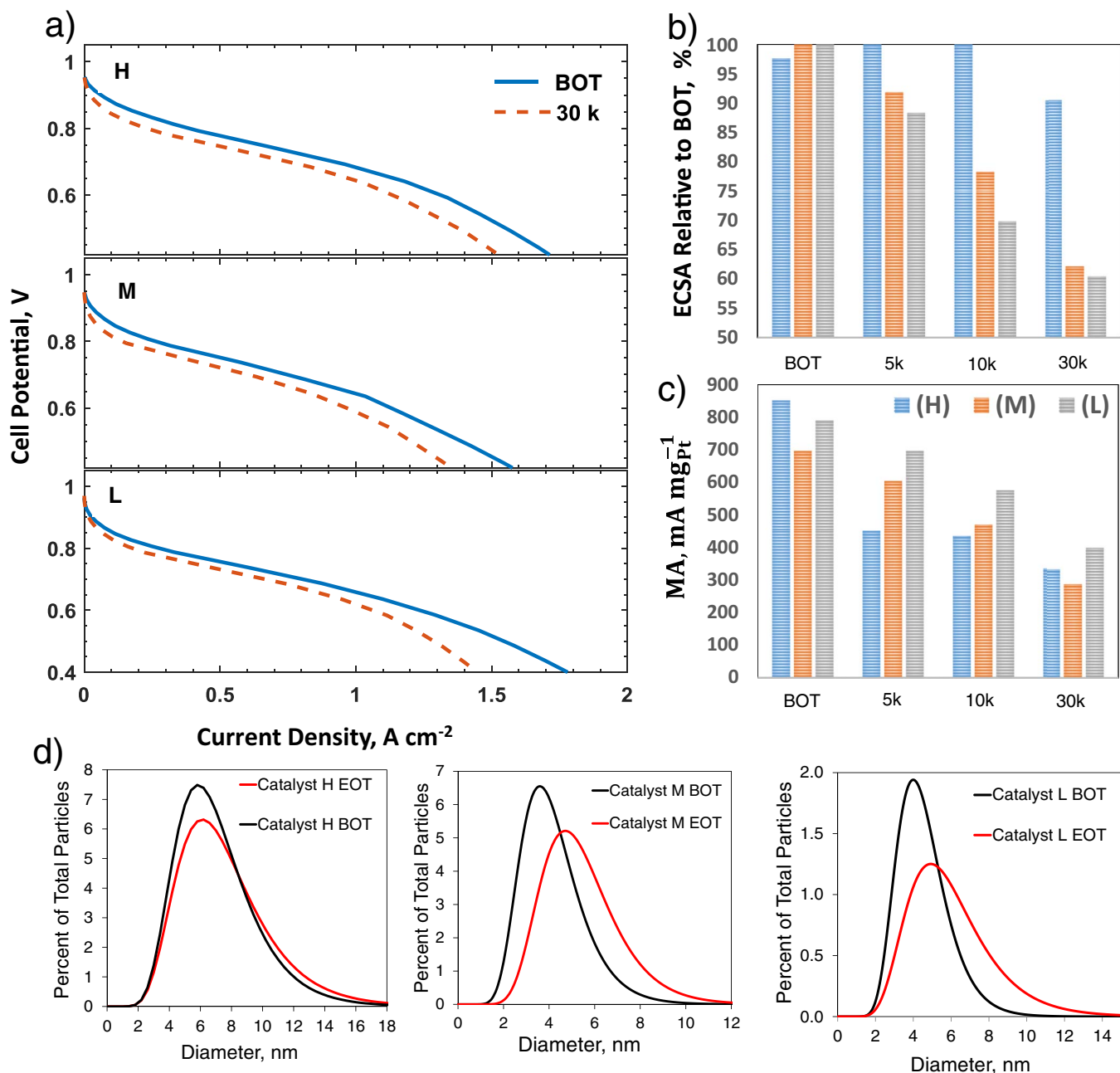
Figure 2. Changes in the MEAs over the course of AST as indicated by a) polarization curves, b) ECSA c) mass activity (MA), and d) particle size distributions measured by SAXS.

Results and Discussion

Figure 2 shows the changes in the properties of all three MEAs over the course of AST potential cycling. From the measured polarization data, Fig. 2a, the cell voltage at 0.8 A cm^{-2} after 30 k cycles compared to BOT decreased by 32 mV for the Catalyst H cell, 36 mV for the Catalyst M cell, and 27 mV for the Catalyst L cell. The corresponding voltage decreases at 1.5 A cm^{-2} were 90 mV, 121 mV, and 148 mV, respectively, clearly indicating a much higher decrease for the two cells with lower initial Pt loading (M and L). Catalyst H, with an initial mean particle size of ~7 nm, showed virtually no change in ECSA during the 30 k cycles AST, whereas the M and L catalysts with smaller initial mean particle sizes (~4.5 nm) showed ECSA losses of ~40% after 30 k potential cycles, Fig. 2b. The measured mass activity (Fig. 2c) for all three catalysts at BOT significantly

exceeded 440 mA/mg$_{Pt}$, which is the U.S. Department of Energy ORR mass activity target for automotive applications.[1] However, all three catalysts showed significant mass activity losses of 47–61% after 30 k cycles, with the final mass activities approaching values typical of dispersed Pt/C catalysts that have been heat-treated to grow to similar size (5–6 nm).[13]

The bulk, average Pt:Co ratio in the CCLs, as well as the Pt:Co within individual particles as a function of particle size, were measured using STEM-EDS. Changes in the {111} lattice spacing of the fresh and aged catalyst particles (catalysts H, M, L) were measured using WAXS. Figure 2d shows SAXS-determined for the three Pt-Co catalyst (H, M, L) particle size distributions in the CCL for the fresh MEA and after 30 k cycle AST. Catalyst H showed a very small change in the Pt-Co particle size, where the mean particle diameter increased
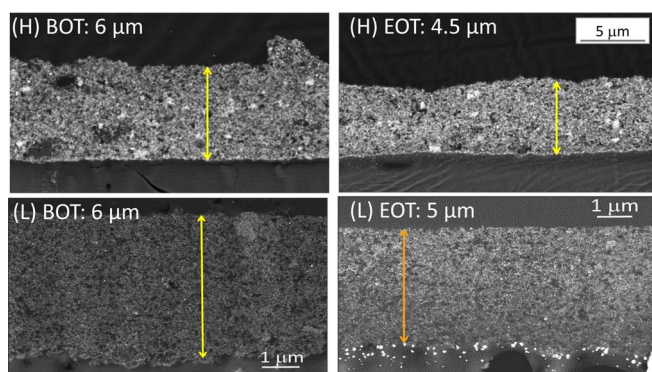
Figure 3. HAADF-STEM cross-section images of CCLs for catalyst H (top left – BOT; top right – EOT) and catalyst L (bottom left – BOT; bottom right – EOT).

from ~7.0 to 7.6 nm as a result of 30 k cycling AST. Catalysts M and L showed increases in the mean Pt-Co particle sizes from 4.4 and 4.5 nm, respectively, to 5.4 and 6.0 nm, respectively. The data indicate more growth of the Pt-Co particles for the catalysts with smaller initial mean diameters (catalysts M and L at BOT), which is also consistent with the observed higher ECSA losses for these catalysts.

Figure 3 shows STEM cross-section images of the CCL's with catalyst H and L compared at BOT and EOT conditions, respectively. The EOT images show measurable thinning of both of the aged CCLs

due to carbon corrosion combined with CCL compaction. CV studies in H_2/N_2 and potentiodynamic studies in H_2/air confirm that the carbon support oxidizes, albeit slowly, to CO_2 under normal fuel cell operating conditions over a potential range of 0.4 to 0.95 V.[14,15] There is also evidence for dissolution of Pt from the CCL, which is supported by the significant amount of Pt precipitation in the membrane adjacent to the CCL.

STEM-EDS data (Fig. 4a) was acquired for individual Pt-Co nanoparticles within the CCLs, both before and after 30 k cycles (BOT and EOT), for catalyst H, M, and L (Fig. 4a show data only for catalyst M, with BOT data shown in blue) and demonstrates that the catalyst nanoparticle composition (Pt:Co) depended on the nanoparticle size at BOT, e.g., larger particles were consistently Co-rich and smaller particles were consistently Pt-rich (this composition-size dependence was similar for all three catalysts, H, M, and L). Significant Co dissolution out of the individual Pt-Co nanoparticles (~40–60%) occurred during the 30 k cycle AST, as compared in Fig. 4a (compare data for BOT in blue to EOT in red) and summarized for all three CCLs in Fig. 4b. It is interesting to note that the data provided in Table I indicated that catalyst powder for H and M had a higher Co content than that measured after incorporation of the same catalyst powders into CCLs and MEAs (note that powders of catalyst L were not available); thus, some Co dissolution from the Pt-Co nanoparticles occurred during electrode and MEA fabrication, as well as during the conditioning/testing step applied prior to the AST.

The average *d*-spacing values calculated from the WAXS (111) peak position for the three catalysts before and after AST cycling (BOT vs. EOT) are shown by the green bars in Fig. 4c, for catalysts
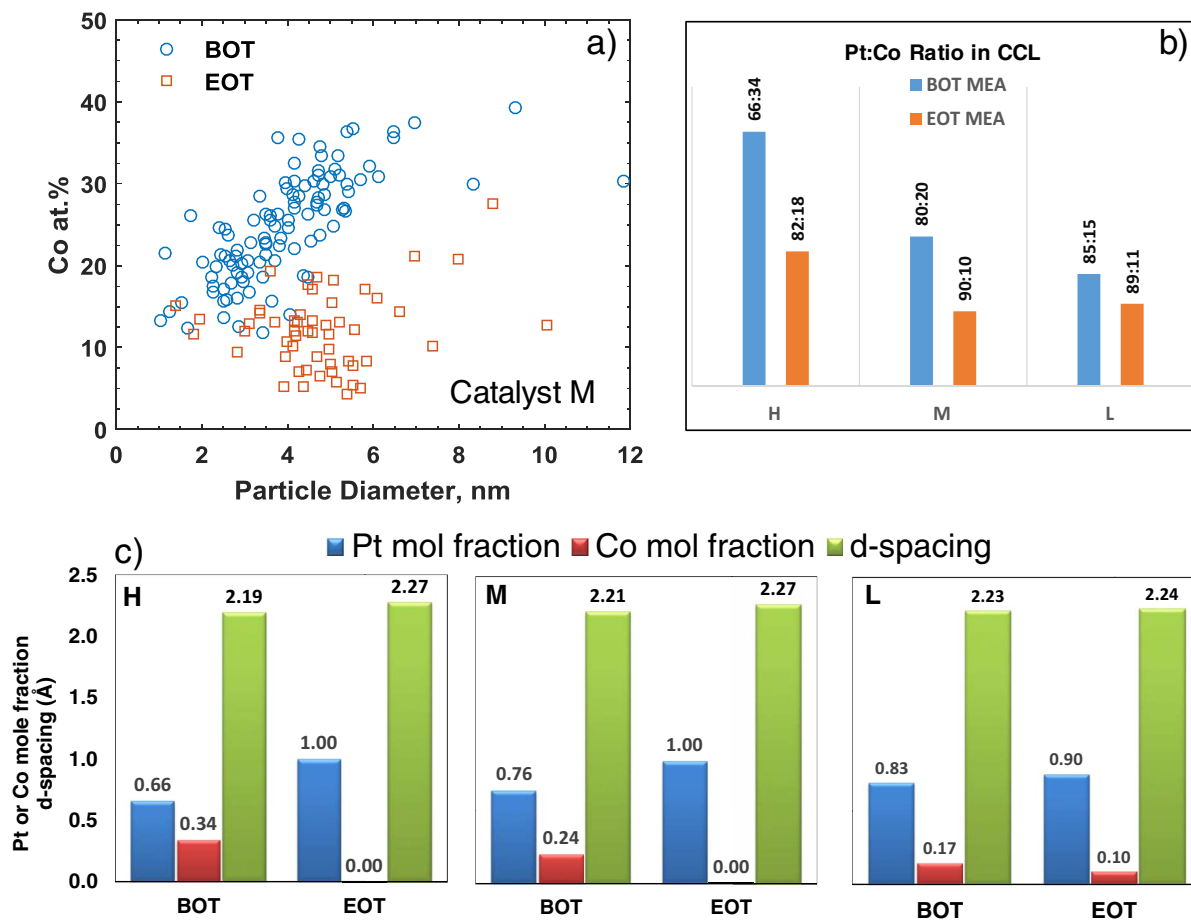
Figure 4. Pt and Co mole fraction in alloy catalysts: a) Nanoparticle composition as function of equivalent particle diameter acquired by STEM-EDS for catalyst M; b) average bulk composition in three CCLs comparing BOT composition to EOT composition determined by STEM-EDS; c) WAXS data acquired from BOT and EOT CCLs with H, M, and L catalysts show Pt and Co mole fractions and (111) *d*-spacings calculated from fit to position of most prominent WAXS (111) peak.

H, M, and L, respectively. The average Pt (blue bars) and Co (red bars) molar ratios were calculated from the acquired *d*-spacing values (using Vegard's law) and are also included in Fig. 4c, for catalysts H, M, and L, respectively. These data indicate that the Pt-Pt (111) *d*-spacing for the EOT Pt-Co alloys, most notably catalysts H and M, increased and approached values closer to that for pure Pt due to extensive dissolution of the Co out of the catalyst nanoparticles during the 30k cycling AST; catalyst L, the SOA Pt-Co GM catalyst did not lose as much Co from the nanoparticles percentage-wise during the 30k cycle AST compared to catalysts H and M.

STEM-EDS analysis of cross-sections of the EOT MEAs showed that Co is found in the ionomer in the CCL and in the membrane in equivalent amounts, however, Co was not found in the anode catalyst layer.

A formal methodology to analyze the polarization data was implemented to infer the effect of aging on proton transport, ORR, and O_2 mass-transfer. The starting point was to estimate the CCL ionic conductivity from the known values of I/C, Pt/C and CCL thickness, and Pt oxide coverage and kinetics from the CV data. Next, we used a distributed ORR kinetic model to analyze the polarization data at low current densities to determine the kinetic and ionic overpotentials. In the final step, the complete set of polarization data was analyzed to determine the mass transfer overpotentials at high current densities.

Neglecting O_2 mass transfer effects and anodic overpotentials, the observed cell voltage (E) measured at a low current density (i) can be written as:

$$E = E_N - i R_\Omega^m - i R_\Omega^c - \eta_s^c \qquad [1]$$

$$E_N = E_0 + \frac{RT}{2F} ln \left(p_{H_2} p_{O_2}^{1/2} \right) \qquad [2]$$
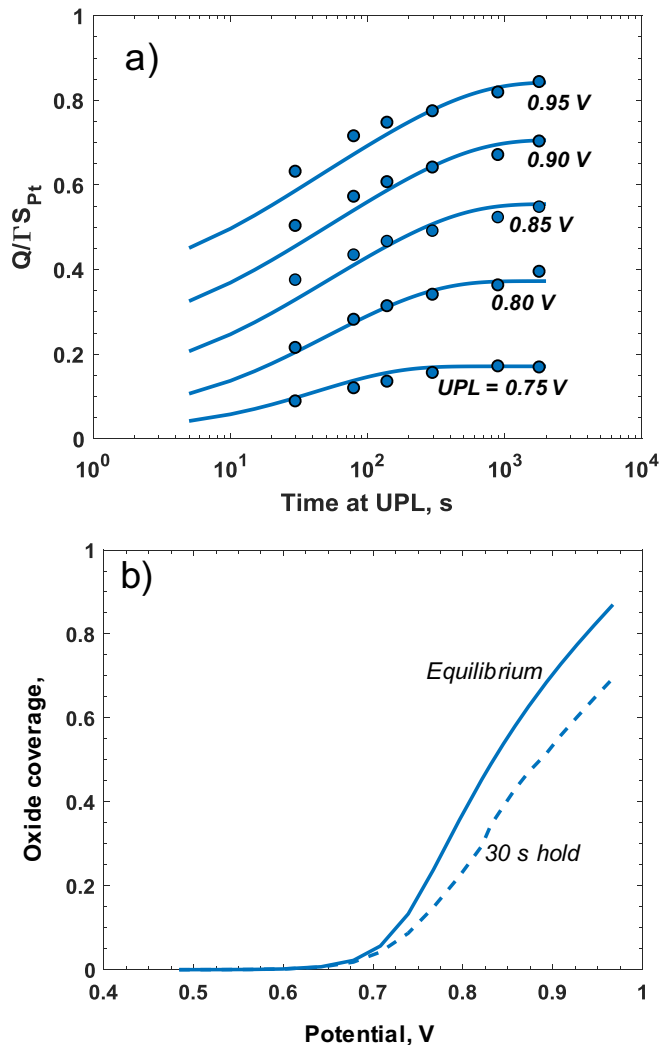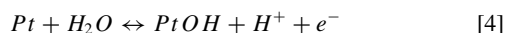
where R_Ω^m is the cell HFR resistance, R_Ω^c is the ionic resistance in the CCL, and η_s^c is the kinetic overpotential for ORR. In this work, we modified the Tafel kinetics model for ORR to incorporate the influence of catalyst surface oxides in blocking O_2 adsorption on Pt sites.[16–18]

$$i + i_x = i_0 S_{Pt} p_{O_2}^\gamma (1 - \theta) e^{-\frac{\omega\theta}{RT}} e^{\frac{\alpha n F}{RT} \eta_s^c} \qquad [3]$$

For oxide-dependent kinetics, the data are consistent with $\alpha n = 0.5$, which corresponds to 140 mV/decade Tafel slope at 80°C and low cathode potentials where $\theta \cong 0$. The effect of ORR inhibition due to surface oxide formation resides in the blocking of available Pt surface sites through the term $(1 - \theta)$ and in altering the adsorption energy of ORR intermediates through a Temkin isotherm energy barrier, ω. In this work, the oxide coverage, θ, is the sum of OH and O formed on Pt as discussed below.

Oxide formation.—The electrochemical surface oxidation of Pt electrodes occurs at potentials >0.7 V. While polycrystalline Pt is known to form stable platinum oxide species (PtO_x) as well as protonated intermediates (Pt_xOH), the nature of the oxide growth on Pt electrodes is still much in debate.[19–24] Studies using X-ray photoelectron spectroscopy combined with density functional theory (DFT) and Monte Carlo simulation have identified various types of adsorbed species as a function of electrochemical potential.[20,25–27] At low potentials, E < 0.60 V, H_2O appears to be the dominant surface species. Above 0.70 V, the hydroxyl group, OH, begins to appear from the oxidation of H_2O. At still higher potentials, OH is further oxidized to O on the catalyst surface. For the higher surface coverages achieved at steady-state potentials above 1.05 V, or for long times at higher potentials, O adsorbs onto higher coordinated subsurface sites resulting from the place-exchange of Pt and O and the formation of an α-PtO_2-like oxide.[25]

On the basis of this literature data, the fractional coverages of Pt oxides formed at potentials up to 0.95 V were determined by considering two consecutive reactions.

$$Pt + H_2O \leftrightarrow PtOH + H^+ + e^- \qquad [4]$$

a) 0.95 V, 0.90 V, 0.85 V, 0.80 V, UPL = 0.75 V

b) Equilibrium, 30 s hold

Figure 5. a) Experimental (symbols)[28] and modeled (line) oxide charge as function of potentiostatic hold time for PtCo alloy; b) comparison of oxide coverage at equilibrium conditions vs. polarization experiments with 30 s hold at each data point.

$$PtOH + H_2O \leftrightarrow PtO + H^+ + e^- \qquad [5]$$

As in previous work, the reaction constants were derived by analyzing the reduction charges measured in CV traces obtained after long potentiostatic holds. We used the data reported by Arisetty et al.[28] who measured the reduction charges for Pt/C and PtCo/C catalysts as function of hold time and potential in a N_2/H_2 atmosphere at 80°C and 100% RH. Figure 5a shows their data for holds at 0.75–0.95 V for times up to 2 h, and cathodically reducing the oxides by scanning back to 0.05 V.

We regard the oxide formed after the 2-h hold as pseudo-steady-state (or "pseudo-equilibrium"), recognizing that Pt may continue to oxidize beyond this time, albeit at a diminishing rate. We define the equilibrium constants for Reactions 4, 5 as follows.

$$K_1 = \left(\frac{\theta_{OH}}{\theta_{Pt}} \right) e^{-\frac{F}{RT}[E_c - E_{01}]} = K_{10} e^{-\frac{\omega_{OH}}{RT} \theta_{OH}^{x_1}} \qquad [6]$$

$$K_2 = \left(\frac{\theta_O}{\theta_{OH}} \right) e^{-\frac{F}{RT}[E_c - E_{02}]} = K_{20} e^{-\frac{\omega_O}{RT} \theta_O^{x_2}} \qquad [7]$$

Here, θ_i denotes the fraction of Pt sites that are free or occupied by OH and oxide species. We let the equilibrium expression be

Table II. Parameters for PtCo oxide formation.

Parameter	Symbol	Value	Unit
Equilibrium constant, PtOH	K_{10}	17.41×10^{-2}	
Equilibrium constant, PtO	K_{20}	10.69×10^{-2}	
Equilibrium potential, PtOH	E_{01}	0.76	V
Equilibrium potential, PtO	E_{02}	1.22	V
Pt to PtOH oxidation rate	$k_{1,f}$	8.91×10^{-5}	A cm^{-2}
PtOH to PtO oxidation rate	$k_{2,f}$	5.58×10^{-3}	A cm^{-2}
Roughness	S_{Pt}	80	cm^2$_{Pt}$ cm^{-2}
Isotherm reaction order, θ_{OH}	x_1	2	
Isotherm reaction order, θ_O	x_2	1	
Anodic transfer coefficient, Pt to PtOH	α_1	0.735	
Anodic transfer coefficient, PtOH to PtO	α_2	0.6	
Temkin parameter, PtOH solution	ω_{OH}	15.74	kJ mol^{-1} K^{-1}
Temkin parameter, PtO solution	ω_O	7.87	kJ mol^{-1} K^{-1}
Pt to PtO interaction parameter	ω_1	24.40	kJ mol^{-1} K^{-1}
PtOH to PtO interaction parameter	ω_2	1.59	kJ mol^{-1} K^{-1}

coverage-dependent through the energy, ω, accounting for oxide interactions on the surface. Table II lists the constants K_{10}, K_{20}, ω_{OH}, ω_O, x_1, and x_2, determined to match the reduction charges measured after 2-h holds at different potentials (Fig. 6a). Figure 6b compares the modeled equilibrium extent of Pt oxidation ($\theta = \theta_{OH} + \theta_O$) for PtCo/C and Pt/C catalysts, assuming that only PtOH and PtO form at these potentials. It clearly shows higher oxidation of Pt in PtCo/C than in Pt/C, indicating that while Pt in the alloy catalyst is more active for ORR, it also forms thicker oxides.

Next, we determined the kinetic constants for Reactions 4 and 5 by comparing oxide formation at different potentials and variable hold times between 30 s and 2 h. This was necessary as the equilibrium Pt oxide coverage cannot be directly used to analyze the polarization curves obtained at fast scan rates. The Pt oxidation currents ($I_{PtOH,}$ and I_{PtO}) were represented by the following equations that reduce to Eqs. 6–7 in the equilibrium limit,

$$I_{PtOH} = k_{1f} e^{\left(\frac{-\omega_1}{RT}\theta_{OH}\right)} \left[\theta_{Pt} e^{\left(\frac{\alpha_1 F}{RT}(E_c - E_{01})\right)} - \frac{\theta_{OH}}{K_1} e^{\left(-\frac{(1-\alpha_1)F}{RT}(E_c - E_{01})\right)} \right]$$
[8]
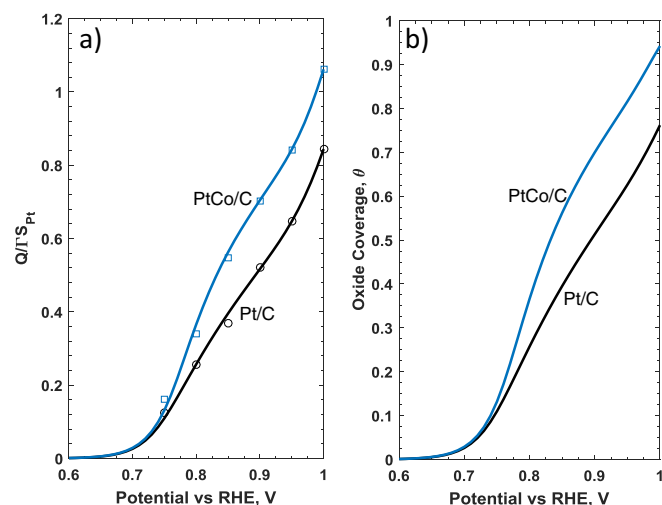
$$I_{PtO} = k_{2f} e^{\left(\frac{-\omega_2}{RT}\theta_O\right)} \left[\theta_{OH} e^{\left(\frac{\alpha_2 F}{RT}(E_c - E_{02})\right)} - \frac{\theta_O}{K_2} e^{\left(-\frac{(1-\alpha_2)F}{RT}(E_c - E_{02})\right)} \right]$$
[9]

Here, we assumed that the kinetic constants are functions of oxide coverage. Having defined the reaction rates, the oxide coverage is calculated by solving the following site balance equations,

$$\Gamma S_{Pt} \frac{d\theta_{OH}}{dt} = I_{PtOH} - I_{PtO}$$
[10]

$$\Gamma S_{Pt} \frac{d\theta_O}{dt} = I_{PtO}$$
[11]

$$\theta_{Pt} = 1 - \theta_{OH} - \theta_O$$
[12]

In addition to the data shown in Fig. 5a, we used the current structure in a typical cathodic scan to determine the rate constants, k_{1f}, k_{2f}, ω_1 and ω_2, and these are listed in Table II. Figure 5b presents the oxide coverage calculated from the kinetic model for the increasing voltage scans with 30-s hold times used in the polarization protocol showing that the modeled θ for the increasing voltage scans is ~30% smaller than the corresponding equilibrium values at voltages in the kinetic region.

ORR kinetics.—Even in the absence of O$_2$ mass transfer resistance, the ORR kinetics at high current densities can be highly non-uniform across the cathode thickness because of the ionomer's finite proton conductivity. An analytical solution for the local ORR rate can be derived and is available in the literature for oxide-coverage independent Tafel kinetics.[29] A numerical solution is required for oxide-coverage dependent Tafel kinetics, which can be obtained by solving the following equation for the ionic potential (Φ_i) in the cathode electrode:

$$\nabla(-\sigma_i \nabla \Phi_i) = \frac{i_0}{\delta_c} A_{Pt} L_{Pt} p_{O_2}^\gamma (1 - \theta) e^{-\frac{\omega\theta}{RT}} e^{\frac{\alpha n F}{RT} \eta_s^c}$$
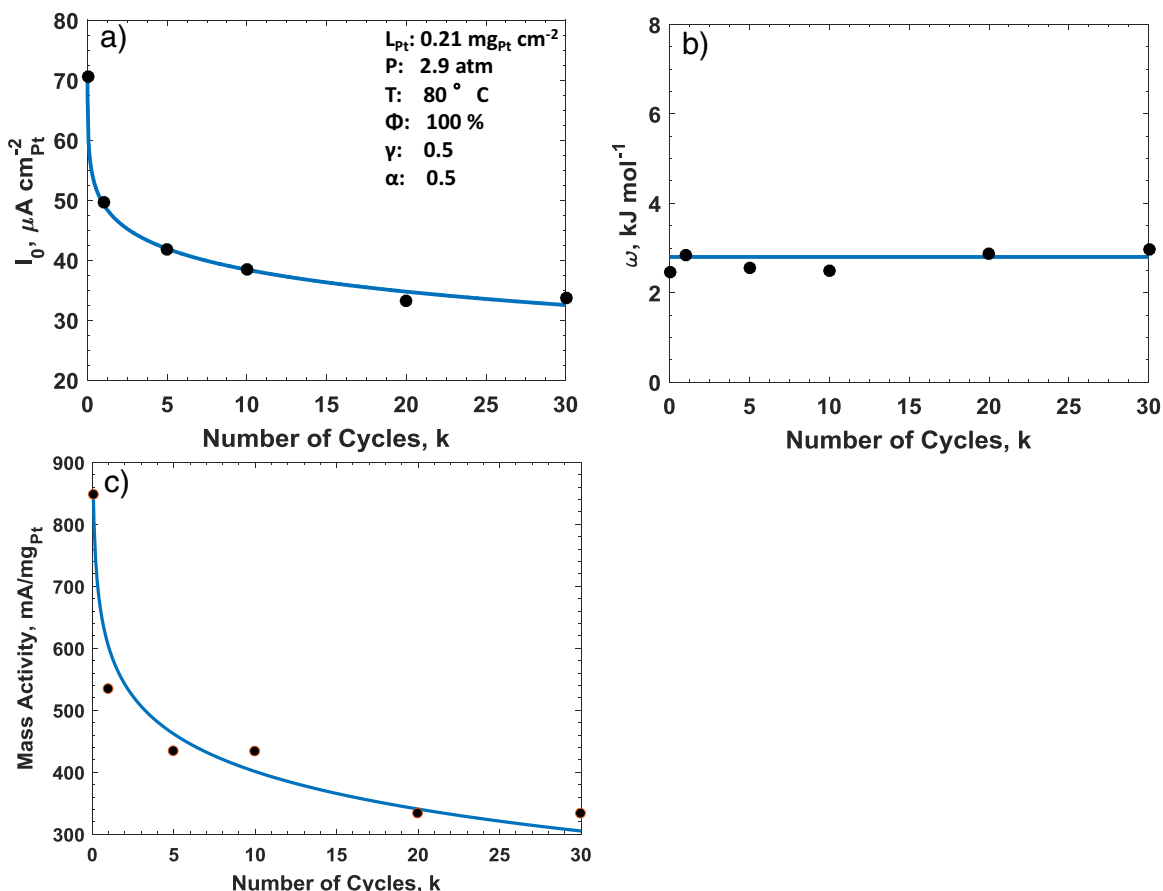[13]

$$\eta_s^c = \Phi_e - \Phi_i - E_N$$
[14]

that are subject to the boundary conditions,

$$-\sigma_i \nabla \Phi_i = \frac{\Phi_i}{R_\Omega^m} \text{ at the membrane/cathode interface}$$
[15]

$$\nabla \Phi_i = 0 \text{ at the GDL/cathode interface}$$
[16]

For convenience, the oxide coverage, θ, evaluated by solving Eqs. 10–12 for 30 s hold at potential was fitted to the following

Figure 6. a) Experimental[28] (symbols) and modeled oxide charge (lines) as function of potential, Q is the charge (C/cm^2), Γ is 210 μC/cm$^2_{Pt}$, S$_{Pt}$ is roughness (cm$^2_{Pt}$/cm^2); b) Pt oxide coverage in Pt/C and PtCo/C catalysts.

Figure 7. Kinetic parameters as function of aging for catalyst H: a) exchange current density, b) Temkin isotherm energy barrier; c) mass activity.

equation:

$$\frac{1}{\theta} = 1 + e^{13.82(0.8799-(\Phi_e - \Phi_i))} \qquad [17]$$

Assuming that $\sigma_i \ll \sigma_e$ so that $\Phi_e = E$, we used the above model to determine the ORR kinetic constants for the three catalysts using the polarization data at low current densities (<0.5 A.cm^{-2}) where the mass transfer effects can be neglected. A regression analysis was conducted to determine i_0 and ω for specified αn and γ and known $\theta(E)$ (see Fig. 6b) and measured ECSA (A_{Pt}) changes with cycles. Figure 7 presents the derived changes in kinetic constants, i_0 and ω, for catalyst H with aging. The exchange current density (i_0) in Fig. 7a declines sharply over the first 1000 cycles and more gradually thereafter. Figure 7b shows only a small change in the degree (ω) to which the surface oxides inhibit ORR kinetics. Considering the moderate growth in particle size observed for this catalyst (7.1 nm to 7.6 nm; see Fig. 2), we conclude that the decrease in i_0 may be attributed primarily to the leaching of Co from the catalyst. Figure 7c shows a good agreement between the mass activities measured in H$_2$/O$_2$ and the values calculated from the ORR kinetic model (with constants derived from H$_2$/air polarization data) for 0.9 V IR-corrected cell voltage, P(O$_2$) = 1 atm, and 100% RH. Only 10% of the degradation in mass activity for Catalyst H is due to ECSA loss, the remaining 90% is likely caused by extensive leaching of the TM out of the alloy.

Figure 8a presents the modeled increase in ORR kinetic overpotential (η_s^c) with aging of Catalyst H. After 30k potential cycles that results in 10% ECSA loss and $\sim$50% leaching of Co, the model indicates that η_s^c has increased by 32 mV at 0.1 A cm^{-2} and by 54 mV at 1.5 A cm^{-2}. Included in Fig. 8 for comparison are the modeled η_s^c for catalysts L and M. We find that the modeled ORR kinetic losses depend on specific activity, ECSA, catalyst loading, Co-content and kinetic parameters (such as catalyst particle morphology). The cata-

lyst H electrode showed the smallest η_s^c due its high initial Pt loading, but had the fastest increase in η_s^c with aging because of low Co retention in the electrode. The L-catalyst electrode showed higher η_s^c due to lower Pt loading, but had a smaller increase in η_s^c with AST cycling because of the higher Co retention and lower overall contraction of the crystalline lattice with cycling, as evidenced by the WAXS data (Fig. 4c). For catalyst L, the increase in η_s^c is primarily due to loss of ECSA during AST cycling. The M-catalyst electrode showed a similar increase in η_s^c with AST cycling as the L-catalyst electrode, but this increase was due to the combined effects of Co dissolution and ECSA loss.

Assuming a linear relationship, Fig. 8d summarizes the effect of Co dissolution on the loss in specific activity for ORR. The data suggest that the specific activity depends not only on the initial Co content of the catalyst, but also on the starting catalyst nanoparticle morphology and size. Even with 27–50% Co loss measured following the 30k cycle ASTs, the specific activity of the three Pt-Co alloy catalysts remains higher than 1000 μA/cm^2-Pt, and exceeds the activity (650 μA/cm^2-Pt) of pure Pt of similar particle size. The measured specific activities are consistent with the ORR kinetic model and catalyst-specific choice of kinetic parameters.

Electrode resistance.—In the absence of mass transfer effects, Neyerlin et al.[29] showed that the effective proton resistance of the CCL, R_Ω^c, can be related to the sheet resistance (R_s^c) by the following equation,[21]

$$R_\Omega^c = \frac{R_s^c}{(3+\zeta)} = \frac{\delta_c}{(3+\zeta)\sigma_i} \qquad [18]$$

where ζ is a correction factor that accounts for catalyst utilization. At low current densities, $\zeta \approx 0$ so that the ORR reaction rate is nearly uniform across the CCL, and R_Ω^c approaches one-third of the sheet
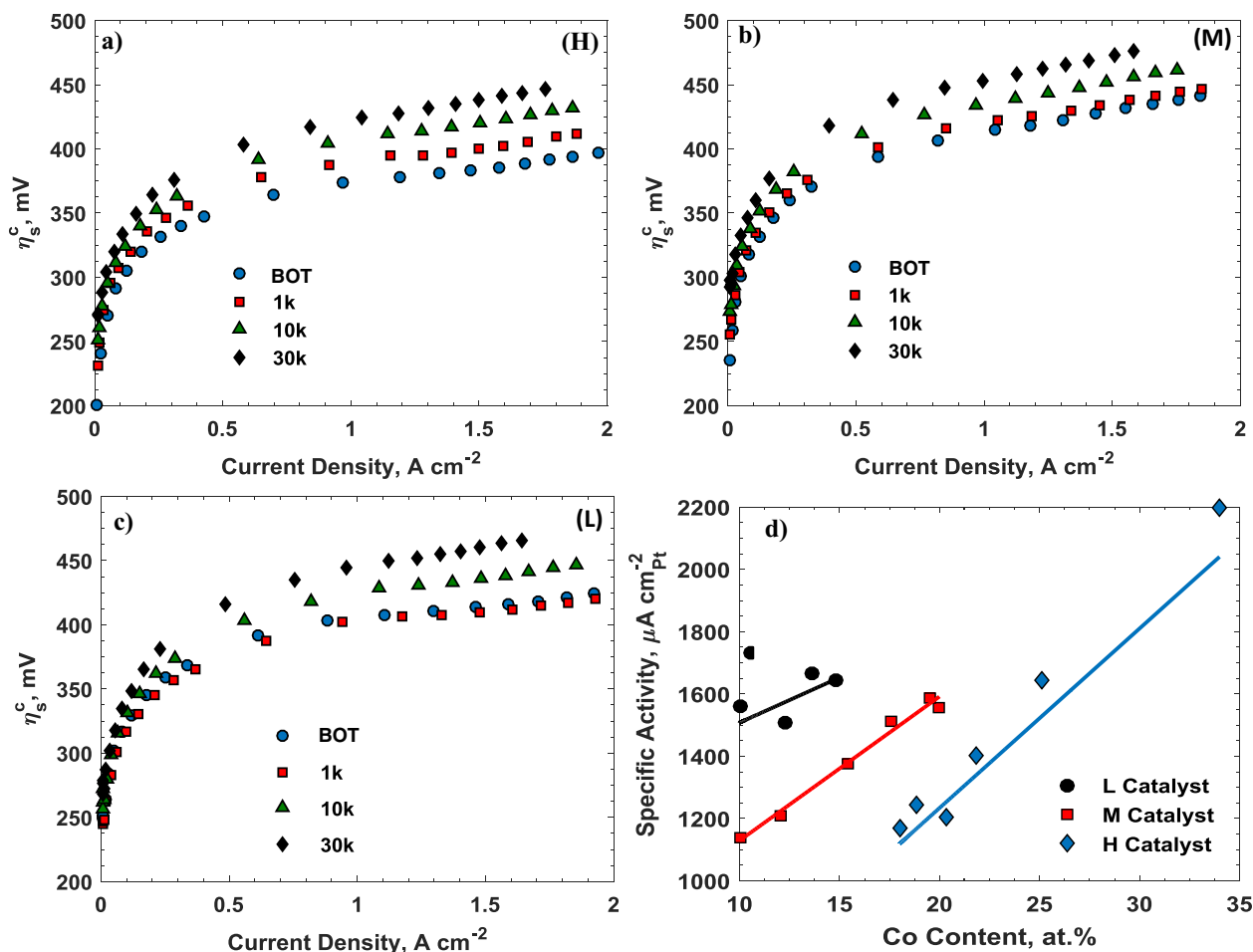
Figure 8. a-c) Overpotentials for catalysts H, M and L; d) specific activity as function of Co content.

resistance. At high current densities, ζ becomes large, and the ORR reaction shifts toward the membrane-electrode interface.

For oxide-coverage dependent Tafel kinetics, Fig. 9a shows the distribution of θ for different cell voltages. Close to OCV (0.9 V), θ is large and varies within a narrow range between 0.5 and 0.6. At lower potentials, 0.7–0.8 V, θ is smaller and highly non-uniform, especially near the membrane-electrode interface.

Figure 9b quantifies the effect of θ and its distribution on ζ as a function of the non-dimensional parameter, $i R_s^c/b$. It includes, for comparison, calculated ζ corresponding to average θ for which the analytical solution also applies. The two sets of results overlap for small values of $i R_s^c/b$ for which the θ variation across the CCL is insignificant and diverge for large values of $i R_s^c/b$ for which θ varies significantly across the CCL.

Figure 9c compares the BOT electrode resistances of the three catalysts. In calculating R_Ω^c, we used the Bruggeman equation[30,31] for estimating the effective electrode proton conductivity (σ_i) from the bulk conductivity (σ_i^m) of the ionomer and the ionomer volume fraction (ε_I) in the electrode:

$$\sigma_i = \sigma_i^m \varepsilon_I^{1.5} \qquad [19]$$

We have used the following equation to estimate ε_I from the ionomer to carbon ratio, Pt to carbon ratio, ionomer density and Pt loading in the electrode (L_{Pt}):

$$\varepsilon_I = \left(\frac{I/C}{Pt/C} \right) \frac{L_{Pt}}{\rho_I \delta_c} \qquad [20]$$

The estimated R_Ω^c in Fig. 9c is largest for catalyst H as it has the lowest I/C. R_Ω^c is smaller for catalyst L than catalyst M, even though the Pt

loadings are similar for M and L; however, the in-house prepared MEA with catalyst M was much thicker.

As noted earlier, all three CCLs showed thinning and collapse of secondary pore structures after being subjected to 30k potential cycles. Figure 9d shows the effect of aging on R_Ω^c due to the measured changes in thickness of the catalyst-H electrode.

Oxygen mass transport.—Having characterized the ORR kinetics and electrode resistance, the overpotential due to O$_2$ mass transport resistance in the gas channel, diffusion medium and CCL (η_m) can be estimated from the voltage balance equation.

$$\eta_m = E_N - i R_\Omega^m - i R_\Omega^c - \eta_s^c - E \qquad [21]$$

The reinforced membrane used for the MEA with catalyst H remained healthy with aging, in that the H$_2$ crossover did not increase significantly, and the measured HFR in Fig. 10 is nearly constant and unaffected by Co^{2+} uptake. Nafion 211 and DuPont XL-100 membranes used with electrodes M and L exhibited similar behavior.

Figure 11a summarizes the inferred η_m for the catalyst H CCL as a function of current density and aging. As expected, η_m is small for current densities below ~0.8 A cm^{-2} and increases rapidly at higher current densities. After 30k cycles, η_m has increased by ~47 mV at 1.5 A cm^{-2}. We see similar trends in Fig. 11b for electrode M and in Fig. 11c for electrode L.

The data in Fig. 11 does not present any clear evidence of a relationship between Co dissolution and a consequent increase in η_m at 100% RH. Catalyst L has the lowest initial Co content and maximum Co retention, but shows the highest increase in η_m after cycling.
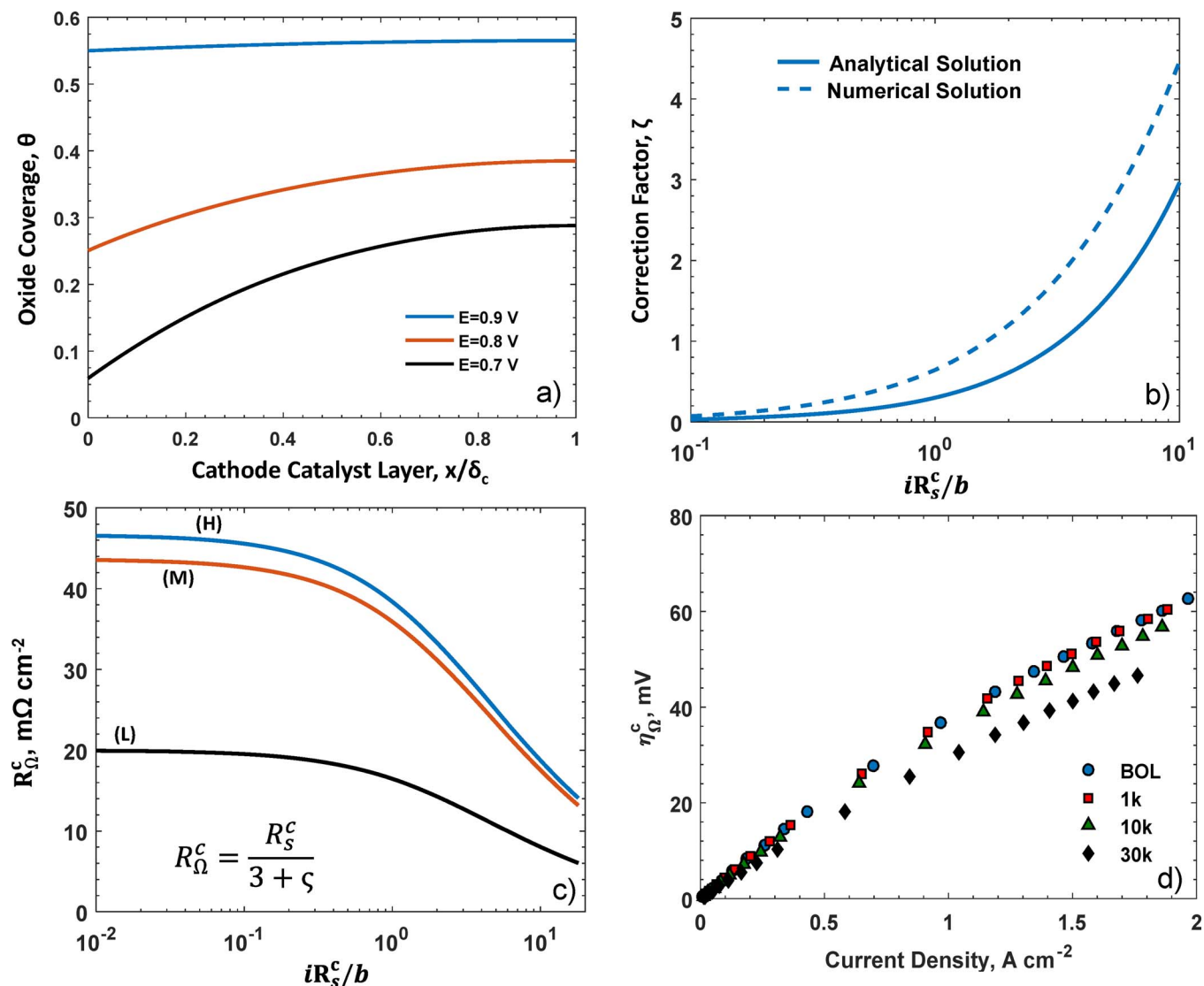
Figure 9. a) Oxide coverage distribution across CCL as function of cell potential (catalyst M); b) Comparison of correction factor for catalyst utilization based on numerical (oxide coverage kinetics) vs. analytical solution (Tafel kinetics); c) CCL resistance at BOT for catalysts H, M and L; d) CCL ionic overpotential for catalyst H catalyst as a function of aging.

Conversely, the catalyst H has the highest initial Co content and lowest Co retention, but shows the smallest increase in η_m after cycling.

As with pure Pt catalysts, we do see a correlation between η_m and Pt roughness (S_{Pt}) defined as the product of Pt loading and the ECSA. We suggest that the catalyst H CCL has the smallest initial η_m and the increase in η_m with aging occurs because it has the highest initial Pt loading and, therefore, highest S_{Pt}. As substantiation, we present the changes in the limiting current density (i_L) for the three electrodes in Fig. 11d. Here, i_L is defined, for convenience, as the current density at which η_m equals 450 mV and varies inversely with the O$_2$ mass transfer resistance ($i_L = 4FC_{O_2}/R_m$). Figure 11d shows that over the limited range of data, i_L correlates with the initial S_{Pt} and the decrease in S_{Pt} due to ECSA loss (Note that whereas is $R_m \infty S_{Pt}$, $i_L \infty S_{Pt}$). The i_L correlation is nearly the same for catalysts L and M that have similar crystalline, fully alloyed nanoparticle morphologies and mean sizes; the small differences in i_L behavior of catalyst H can be attributed to its spongy (porous) morphology. The catalyst H electrode also shows a much lower i_L than expected from the trends observed for catalyst L and M electrodes, and the larger roughness factor. Other studies have shown catalyst-specific relationships between η_m and the reduced current density, i/i_L, that quantify the increase in η_m with a

decrease in either initial Pt loading or decrease in ECSA caused by potential cycling.

Breakdown of overpotentials.—Figure 12 provides a breakdown of the change in overpotentials with aging of the three MEAs at 1.5 A cm^{-2}. After 30k cycles, the H electrode has the smallest increase in total overpotential (90 mV), followed by M (121 mV) and L electrodes (148 mV).

At 100% RH, the ohmic overpotentials ($\eta_\Omega^m = i R_\Omega^m$) depend on the membrane used but do not change significantly with potential cycling in spite of significant leaching of Co from catalysts M and H, some of which migrates into the membrane. The modeled ionic overpotential in the CCL includes the effect of compaction/thinning but not any compensating reduction of σ_i due to Co^{2+} ion exchanging with H$^+$ in the ionomer. This poisoning effect is likely small because the HFR did not increase due to Co^{2+} uptake in the membrane, and, due to the analysis method used, is included in η_s^c.

Assuming that Co^{2+} leached from the catalyst exchanges equally with H$^+$ in the sulfonic acid groups in the ionomer and in the membrane and neglecting any concentration gradients, we estimate that, after 30k cycles, Co^{2+} occupies 26% of the proton sites in the H
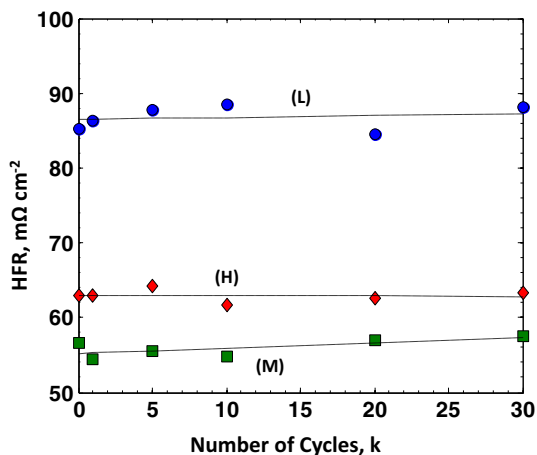
Figure 10. HFR at 1 A cm^{-2} as a function of potential cycling.

electrode, 6.5% in the M electrode, and 1.1% in the L electrode. Under potential gradients, however, Co^{2+} ions are likely to migrate from the membrane to the CCL resulting in significantly higher Co^{2+} contamination of the cathode ionomer than these estimates.

The majority of the increase in voltage losses are due to comparable changes in kinetic and mass transfer overpotentials. As discussed earlier, the increase in η_s^c is related to the initial Pt loading, ECSA loss, Co retention and also the catalyst morphology. At 100% RH, the

increase in η_s^c after 30k cycles is largest for H electrode (54 mV) and comparable for M electrode (43 mV) and L electrode (46 mV).

The increase in η_m is primarily related to the initial Pt loading and ECSA loss, and Co leaching into the ionomer is only a secondary factor. At 100% RH, the increase in η_m after 30k cycles is smallest for H electrode (45 mV) and larger for M electrode (86 mV) and L electrode (106 mV).

As a perspective, we compare our results with data from some literature studies in which fresh MEAs were purposely doped with transition metal ion impurities. Greszler et al.[33] measured losses in stack voltage that were minor for up to 30% Co^{2+} site occupancy under humidified conditions (110% RH at outlet), but substantial for dry operation (80% RH at outlet). With Ni^{2+} as the contaminant, Sulek et al.[34] observed quantifiable losses in cell voltage at 100% RH with only 10% site occupancy, and much higher transport-related losses at 30% site occupancy. Finally, Braaten et al.[35] measured limiting currents and deduced enhanced oxygen transport resistances that scale with Co^{2+} site occupancy (5–100%) and are much higher if the operating conditions are dry (40% RH) rather than wet (100% RH).

Conclusions

We have investigated the durability of three SOA Pt-Co alloy cathode catalysts under cyclic potentials. STEM-EDS and WAXS data confirm that Co in the catalysts is unstable at the operating fuel cell potentials, and leaches out of the cathode catalyst and into the ionomer. Even with significant (27–50%) Co loss, the specific activity of all the Pt-Co alloy catalysts for ORR remains higher than 1000 μA/cm^2-Pt, and exceeds the activity (650 μA/cm^2-Pt) of pure Pt of similar
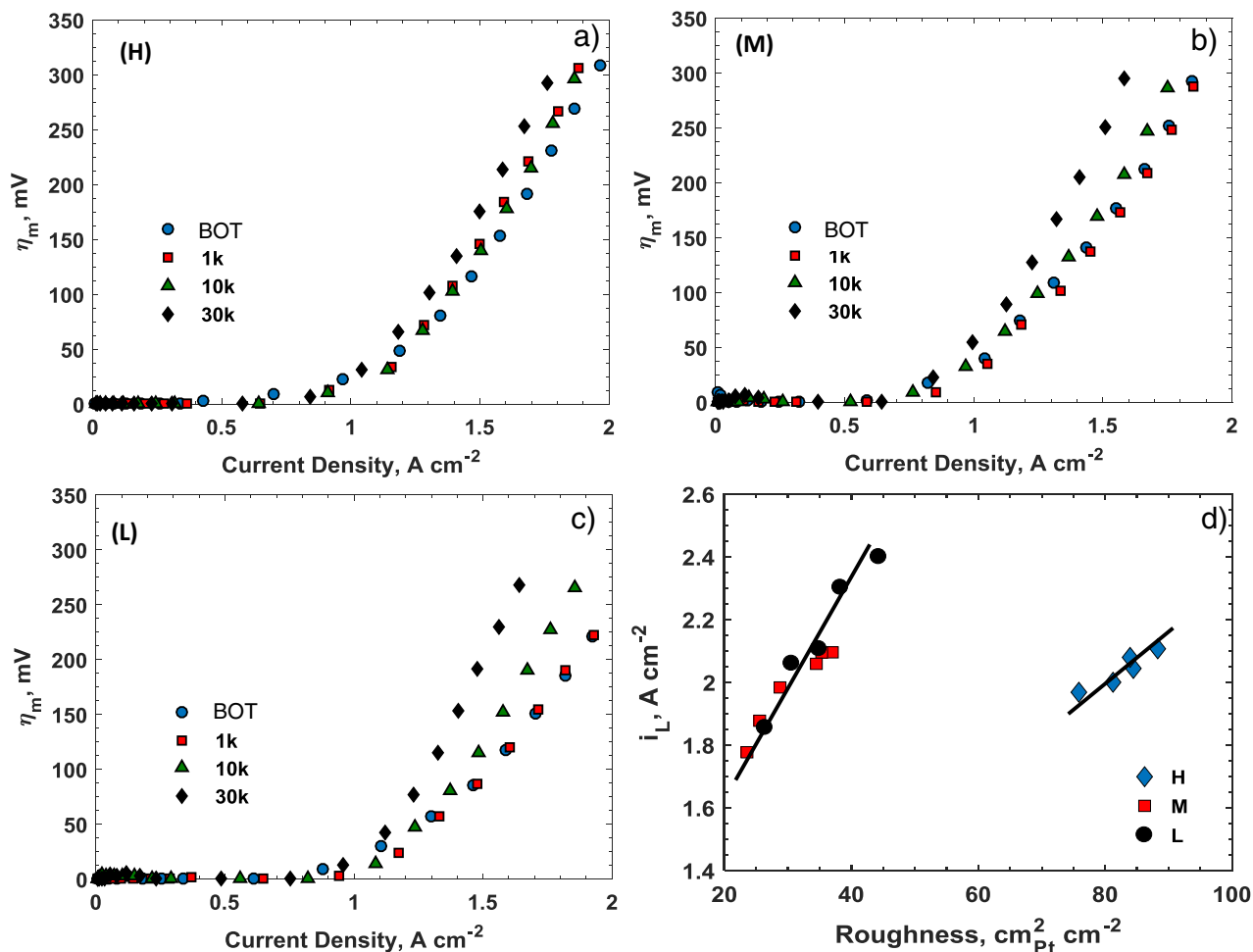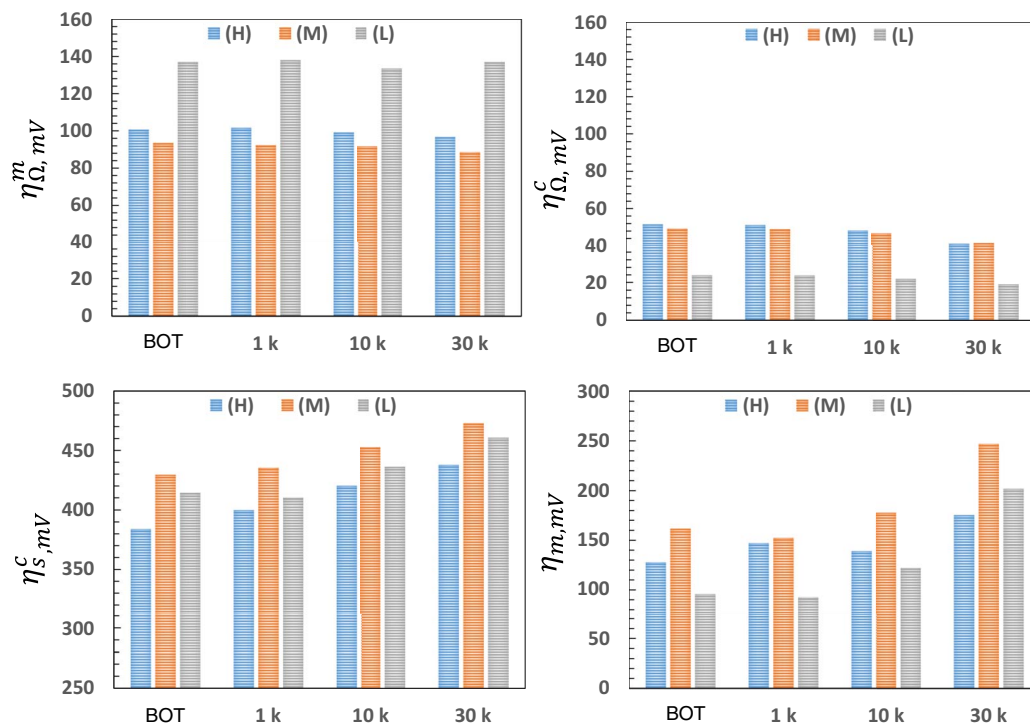

Figure 11. a-c) Mass transfer overpotentials for catalysts H, M, and L; d) limiting current density as a function of roughness.

Figure 12. Breakdown of change in overpotentials with aging at 1.5 A cm^{-2}.

particle size. The measured specific activities are consistent with a kinetic model and catalyst-specific choice of kinetic parameters.

The majority of the observed voltage losses with aging are due to increased kinetic and mass transfer losses. In spite of substantial Co^{2+} uptake in the CCL ionomer and the membrane, the measured HFR and modeled electrode ionic resistance do not show significant changes at 100% RH.

The ORR kinetic losses depend on specific activity, ECSA, Pt loading, initial Co content and the catalyst morphology. The observed increase in the kinetic overpotentials with aging were due to low Co retention in the spongy catalyst with high initial Co content, ECSA loss in the fully alloyed crystalline catalyst with low initial Co content, and combined effects of Co dissolution and ECSA loss in the crystalline catalyst with medium Co content.

The modeled increase in mass transfer overpotentials with aging correlates with Pt loading and ECSA loss and depends on the initial catalyst morphology. There is no clear evidence of a relationship between Co dissolution (i.e., effect of Co^{2+} on O$_2$ permeability in ionomer film) and the resulting increase in η_m at 100% RH. However, Co dissolution contributes to ECSA loss. As with pure Pt catalysts, we see a correlation between η_m and Pt roughness (cm^2_{Pt}/cm^2) which is defined as the product of Pt loading and ECSA.

Further work is required to extend the combined experimental and analytical methodology presented here to investigate the stability of the alloy catalyst under different potential cycles with variable potential limits and scan rates and to differentiate the effect of resulting Co^{2+} contamination on concentration polarization, ORR kinetics and O$_2$ mass transport overpotentials, particularly under dry conditions.

List of Symbols

a	Activity coefficient
b	Tafel slope
E	Potential
F	Faraday constant
i	Current density
k	Kinetic constant
K	Equilibrium constant
L	Pt loading
M	Molecular mass

n	Number of electrons
p	Partial pressure
R	Gas constant, resistance, ratio
S	Surface roughness

Greek

α	Electron transfer coefficient
γ	O_2 partial pressure dependence
Γ	Specific charge in the hydrogen adsorption region
δ	Thickness of cathode catalyst layer
ε	Porosity
ζ	Utilization factor
η	Overpotential
θ	Oxide coverage
ρ	Density
σ	Conductivity
ω	Energy parameter for oxide adsorption
Ω	ohmic

Subscripts and Superscripts

0	Standard
c	Cathode
e	Effective, electronic
i	Ionic
I/C	Cathode ionomer to carbon mass fraction
m	Mass-transfer or membrane
Pt/C	Cathode Pt to carbon mass fraction
N	Nernst
s	Activation
x	Cross-over

ORCID

D. D. Papadias https://orcid.org/0000-0003-1187-6502
R. K. Ahluwalia https://orcid.org/0000-0002-9031-1907
D. Myers https://orcid.org/0000-0001-9299-3916
K. L. More https://orcid.org/0000-0001-5223-9097
R. Mukundan https://orcid.org/0000-0002-5679-3930
R. L. Borup https://orcid.org/0000-0001-7647-1624

References

1. Department of Energy, Fuel Cell Technologies Office Multi-Year Research, Development, and Demonstration Plan, https://energy.gov/eere/fuelcells/fuel-cell-technologies-office.
2. A. Kongkanand and M. F. Mathias, *J Phys Chem Lett*, **7**, 1127 (2016).
3. H. F. Lv, D. G. Li, D. Strmcnik, A. P. Paulikas, N. M. Markovic, and V. R. Stamenkovic, *Nano Energy*, **29**, 149 (2016).
4. N. Konno, S. Mizuno, H. Nakaji, and Y. Ishikawa, *SAE International Journal of Alternative Powertrains*, **4**, 123 (2015).
5. T. Yoshida and K. Kojima, *Electrochem Soc Interface*, **24**, 45 (2015).
6. S. Chen, H. A. Gasteiger, K. Hayakawa, T. Tada, and Y. Shao-Horn, *J Electrochem Soc*, **157**, A82 (2010).
7. L. Dubau, M. Lopez-Haro, L. Castanheira, J. Durst, M. Chatenet, P. Bayle-Guillemaud, L. Guetaz, N. Caque, E. Rossinot, and F. Maillard, *Appl Catal B-Environ*, **142**, 801 (2013).
8. L. Dubau, F. Maillard, M. Chatenet, L. Guetaz, J. Andre, and E. Rossinot, *J Electrochem Soc*, **157**, B1887 (2010).
9. M. Gummalla, S. C. Ball, D. A. Condit, S. Rasouli, K. Yu, P. J. Ferreira, D. J. Myers, and Z. W. Yang, *Catalysts*, **5**, 926 (2015).
10. M. Lopez-Haro, L. Dubau, L. Guetaz, P. Bayle-Guillemaud, M. Chatenet, J. Andre, N. Caque, E. Rossinot, and F. Maillard, *Appl Catal B-Environ*, **152**, 300 (2014).
11. K. More, *DOE Fuel Cell Technologies Office Annual Merit Review*, Washington DC, June 6, 2017 (2017).
12. U.S. DRIVE Partnership, "Fuel Cell Technical Team Roadmap," 2013.
13. D. Myers, N. Kariuki, R. K. Ahluwalia, X. Wang, C. F. Cetinbas, and J. K. Peng, *DOE Fuel Cell Technologies Office Annual Merit Review*, Washington DC, June 6–10, 2016 (2016).
14. R. L. Borup, D. D. Papadias, R. Mukundan, D. Spernjak, D. Langlois, R. K. Ahluwalia, K. More, and S. Grot, *ECS Trans*, **69**, 1029 (2015).
15. A. Pandy, Z. W. Yang, M. Gummalla, V. V. Atrazhev, N. Y. Kuzminyh, V. I. Sultanov, and S. Burlatsky, *J Electrochem Soc*, **160**, F972 (2013).
16. S. Gottesfeld, *ECS Trans*, **25**, 51 (2008).
17. N. P. Subramanian, T. A. Greszler, J. Zhang, W. Gu, and R. Makharia, *J Electrochem Soc*, **159**, B531 (2012).
18. J. X. Wang, N. M. Markovic, and R. R. Adzic, *J Phys Chem B*, **108**, 4127 (2004).
19. H. Angerstein-Kozlowska, B. E. Conway, and W. B. A. Sharp, *J Electroanal Chem Interfacial Electrochem*, **43**, 9 (1973).
20. H. S. Casalongue, S. Kaya, V. Viswanathan, D. J. Miller, D. Friebel, H. A. Hansen, J. K. Norskov, A. Nilsson, and H. Ogasawara, *Nat Commun*, **4** (2013).
21. Y. F. Huang, P. J. Kooyman, and M. T. M. Koper, *Nat Commun*, **7** (2016).
22. G. Jerkiewicz, G. Vatankhah, J. Lessard, M. P. Soriaga, and Y. S. Park, *Electrochim Acta*, **49**, 1451 (2004).
23. E. L. Redmond, B. P. Setzler, F. M. Alamgir, and T. F. Fuller, *Phys Chem Chem Phys*, **16**, 5301 (2014).
24. M. Wakisaka, H. Suzuki, S. Mitsui, H. Uchida, and M. Watanabe, *Langmuir*, **25**, 1897 (2009).
25. H. Imai, K. Izumi, M. Matsumoto, Y. Kubo, K. Kato, and Y. Imai, *J Am Chem Soc*, **131**, 6293 (2009).
26. H. Imai, M. Matsumoto, T. Miyazaki, K. Kato, H. Tanida, and T. Uruga, *Chem Commun*, **47**, 3538 (2011).
27. A. Teliska, W. E. O'Grady, and D. E. Ramaker, *J Phys Chem B*, **109**, 8076 (2005).
28. S. Arisetty, Y. Liu, and M. F. Mathias, *ECS Trans*, **69**, 273 (2015).
29. K. C. Neyerlin, W. Gu, J. Jorne, A. Clark, and H. A. Gasteiger, *J Electrochem Soc*, **154**, B279 (2007).
30. T. E. Springer, T. A. Zawodzinski, and S. Gottesfeld, *J Electrochem Soc*, **138**, 2334 (1991).
31. C. Boyer, S. Gamburzev, O. Velev, S. Srinivasan, and A. J. Appleby, *Electrochim Acta*, **43**, 3703 (1998).
32. A. Ohma, T. Mashio, K. Sato, H. Iden, Y. Ono, K. Sakai, K. Akizuki, S. Takaichi, and K. Shinohara, *Electrochim Acta*, **56**, 10832 (2011).
33. T. A. Greszler, T. E. Moylan, and H. A. Gasteiger, in *Handbook of Fuel Cells – Fundamentals, Technology and Applications*, W. Vielstich, H. A. Gasteiger, A. Lamm, and H. Yokokawa, Editors, John Wiley & Sons, Hoboken, NJ (2010).
34. M. Sulek, J. Adams, S. Kaberline, M. Ricketts, and J. R. Waldecker, *J Power Sources*, **196**, 8967 (2011).
35. J. Braaten, A. Kongkanand, and S. Litster, *ECS Trans*, **80**, 283 (2017).